

# Controlled Micro/Nanodome Formation in Proton-Irradiated Bulk Transition-Metal Dichalcogenides

Davide Tedeschi, Elena Blundo, Marco Felici, Giorgio Pettinari, Boqing Liu, Tanju Yildirim, Elisa Petroni, Chris Zhang, Yi Zhu, Simona Sennato, Yuerui Lu,\* and Antonio Polimeni\*

At the few-atom-thick limit, transition-metal dichalcogenides (TMDs) exhibit strongly interconnected structural and optoelectronic properties. The possibility to tailor the latter by controlling the former is expected to have a great impact on applied and fundamental research. As shown here, proton irradiation deeply affects the surface morphology of bulk TMD crystals. Protons penetrate the top layer, resulting in the production and progressive accumulation of molecular hydrogen in the first interlayer region. This leads to the blistering of one-monolayer thick domes, which stud the crystal surface and locally turn the dark bulk material into an efficient light emitter. The domes are stable (>2-year lifetime) and robust, and host strong, complex strain fields. Lithographic techniques provide a means to engineer the formation process so that the domes can be produced with well-ordered positions and sizes tunable from the nanometer to the micrometer scale, with important prospects for so far unattainable applications.

The notable transformation of the electronic properties of transition-metal dichalcogenides (TMDs) when reduced to a single X–M–X plane (X: chalcogen; M: metal)<sup>[1]</sup> makes them suitable for flexible, innovative optoelectronic devices,<sup>[2–4]</sup> and transistors.<sup>[5]</sup> Like graphene, few-layer TMDs can also withstand surprisingly large mechanical deformations,<sup>[6–9]</sup> which, coupled to the material's electronic structure, would enable the observation of nondissipative topological transport, provided a periodic modulation of strain is attained.<sup>[10–13]</sup> TMD monolayers (MLs) and nanostructures are also important for their catalytic role in the cost-effective production of hydrogen.<sup>[14–16]</sup> These examples share the need to achieve spatial control of

the material's properties, over sample regions with size ranging from the nano<sup>[14,16]</sup> to the micrometer<sup>[16]</sup> scale lengths.

In this study, we present a route toward the patterning of TMDs based on the effects of low-energy proton irradiation<sup>[17]</sup> on the structural and electronic properties of bulk WS<sub>2</sub>, WSe<sub>2</sub>, WTe<sub>2</sub>, MoS<sub>2</sub>, MoSe<sub>2</sub>, and MoTe<sub>2</sub>. Suitable irradiation conditions trigger the production and accumulation of H<sub>2</sub> just beneath the first X–M–X basal plane, leading to the localized exfoliation of the topmost monolayer and to the formation of spherically shaped domes. Structural and optical characterizations confirm that these domes are typically one ML-thick and contain H<sub>2</sub> at pressures in the 10–100 atm range, depending on their size. Such high pressures induce strong and complex strain fields acting on the curved X–M–X planes, that are evaluated by means of a mechanical model. The domes' morphological characteristics can be tuned by lithographically controlling the area of the sample basal plane participating in the hydrogen production process. This results in the unprecedented fabrication of robust domes with controlled position/density and sizes tunable from the nanometer to the micrometer scale, that, by virtue of their inherently strained nature and geometry, might prompt a variety of applications.

The samples, consisting of thick (tens to hundreds of MLs) TMD flakes, were obtained by mechanical exfoliation, deposited on Si substrates, and afterwards proton-irradiated using a Kaufman source (see the Experimental Methods). Differently from the other works in the literature concerning proton-irradiation of TMDs—where beams with energies  $\geq 10^5$  eV are used,<sup>[18]</sup> aiming at the controlled formation of defects in the irradiated samples—here we irradiate the flakes with low energy

Dr. D. Tedeschi, E. Blundo, Prof. M. Felici, E. Petroni, Prof. A. Polimeni  
Dipartimento di Fisica  
Sapienza Università di Roma  
00185 Roma, Italy  
E-mail: antonio.polimeni@roma1.infn.it

Dr. G. Pettinari  
Institute for Photonics and Nanotechnologies  
National Research Council  
00156 Roma, Italy

B. Liu, Dr. T. Yildirim, C. Zhang, Y. Zhu, Prof. Y. Lu  
Research School of Electrical  
Energy and Materials Engineering  
College of Engineering and Computer Science  
The Australian National University  
Canberra ACT2601, Australia  
E-mail: yuerui.lu@anu.edu.au

Dr. T. Yildirim  
College of Chemistry and Environmental Engineering  
Shenzhen University  
P. R. China

Prof. Y. Lu  
ARC Centre of Excellence in Future Low-Energy  
Electronics Technologies (FLEET)  
ANU node  
Canberra ACT2601, Australia

Dr. S. Sennato  
Institute for Complex Systems  
National Research Council  
00185 Roma, Italy

 The ORCID identification number(s) for the author(s) of this article can be found under <https://doi.org/10.1002/adma.201903795>.

DOI: 10.1002/adma.201903795

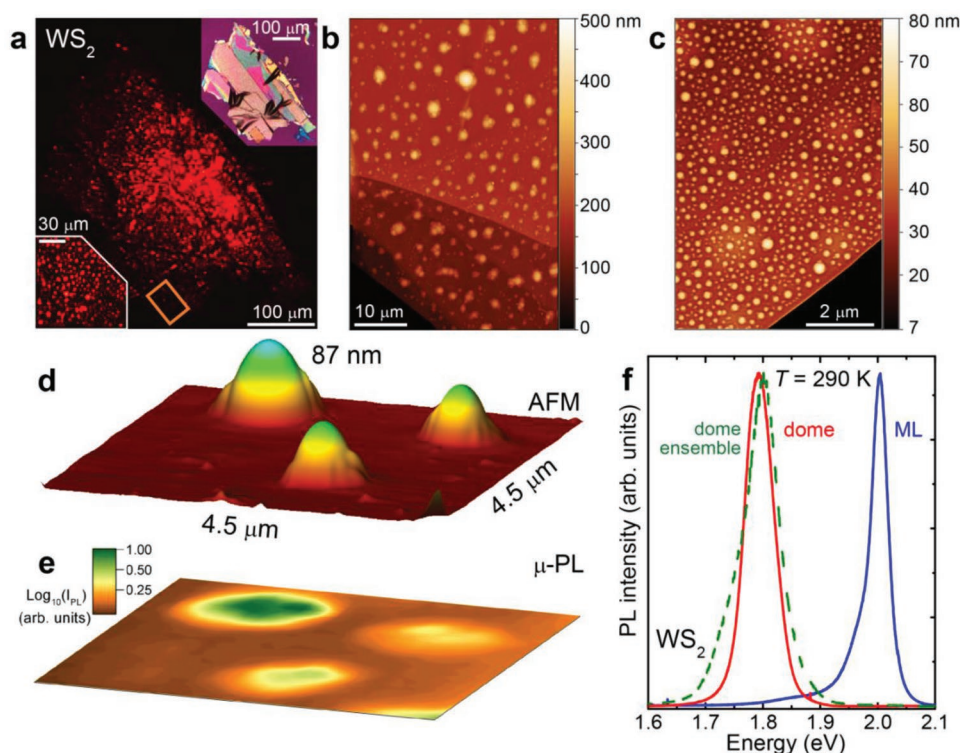


**Figure 1.** Creation of light-emitting domes by proton irradiation. a) Optical microscopy image showing the laser-excited red luminescence of bulk WS<sub>2</sub> after irradiation with proton dose  $d_{\text{H}} = 8 \times 10^{16}$  protons cm<sup>-2</sup>. The top-right inset shows the same flake in absence of laser excitation. The bottom-left inset is a zoomed-in image of the main picture showing the round shape of the emitting spots. b) AFM image of the rectangular region highlighted in (a). Round-shaped features on the sample surface form after H<sup>+</sup> irradiation. c) AFM image of a bulk WS<sub>2</sub> flake H<sup>+</sup>-irradiated with a dose eight times smaller than in (a) and (b). d) AFM image of a limited region of a sample treated like that shown in (c) but on a different flake, where a smaller density of domes was fortuitously found. The maximal height reached by the domes is 87 nm. e)  $\mu$ -PL mapping (detection wavelength equal to 689 nm) of the same region displayed in (d). The base-10 logarithm of the  $\mu$ -PL intensity is shown as a false color scale (see color bar). f)  $\mu$ -PL spectrum of a dome (red line) singled out from the ensemble displayed in (a); the blue line is the  $\mu$ -PL spectrum of a WS<sub>2</sub> monolayer, whereas the green dashed line is the macro-PL spectrum of an ensemble formed by  $\approx 2500$  domes. The spectra are peak normalized for ease of comparison. The dome PL intensity is a factor 7 greater than that of the ML.

beams ( $\leq 20$  eV), with the specific goal of suppressing the defect formation process. The top-right inset of **Figure 1a** displays the optical microscopy image of a large bulk WS<sub>2</sub> sample after irradiation with an impinging dose  $d_{\text{H}} = 8 \times 10^{16}$  protons cm<sup>-2</sup>. Unexpectedly for indirect-gap bulk WS<sub>2</sub>, the sample exhibits strong photoluminescence (PL, see the Experimental Section) in the red wavelength region ( $\lambda \approx 690$  nm), as displayed in the main part of **Figure 1a** and **Figure S1** (Supporting Information). The bottom-left inset shows that the luminescence originates from circular spots with diameters varying between less than one (which is an upper limit due to the finite resolution of our optical setup; see the Experimental Section) to few microns. As is evident from the atomic force microscopy (AFM, see the Experimental Section) image in **Figure 1b**, these spots signal the presence of dome-shaped features, protruding from the irradiated crystal surface, with virtually perfect spherical shape (see **Figure S2** in the Supporting Information). The average footprint radius of the features displayed in **Figure 1b** is  $R = (1.43 \pm 0.12) \mu\text{m}$ —with maximal height  $h_{\text{m}} = (230 \pm 20)$  nm—but the dome size can be controlled by the irradiated proton dose: with  $d_{\text{H}} = 1.0 \times 10^{16}$  protons cm<sup>-2</sup> we obtained nanometer-sized structures, with average  $R = (164 \pm 40)$  nm and  $h_{\text{m}} = (25.6 \pm 5.6)$  nm (**Figure 1c**). **Figure 1d** shows an AFM image encompassing three domes

formed on a WS<sub>2</sub> sample analogous to that shown in **Figure 1c**. The corresponding room temperature micro-PL ( $\mu$ -PL, see the Experimental Section) intensity map, detected at  $\lambda_{\text{det}} = 689$  nm and displayed in **Figure 1e**, demonstrates the perfect match between the domes and the light-emitting spots. The  $\mu$ -PL spectrum of one dome (singled out from the ensemble of **Figure 1a**) is provided in **Figure 1f**. The luminescence of an untreated WS<sub>2</sub> ML measured under the same excitation/collection conditions is shown for comparison. The PL intensity of the domes is typically larger than that of the exfoliated WS<sub>2</sub> MLs, indeed suggesting a one-ML thickness for the domes. This hypothesis is confirmed by measuring the  $\mu$ -PL spectrum and the thickness of the outer layer of exploded domes, which are both fully consistent with that of the monolayer (as exemplified for a MoSe<sub>2</sub> dome in **Figure S3** in the Supporting Information). This is further supported by the strong circular dichroism measured for the PL emission of the domes (in a WS<sub>2</sub> dome the degree of circular polarization is  $>50\%$  at 130 K, see **Figure S4A**, Supporting Information), which is a property stemming directly from the hexagonal symmetry of the first Brillouin zone of monolayered TMDs (see **Figure S4B** in the Supporting Information).<sup>[19]</sup> Likewise, evidence of the one-ML nature of the domes is also provided by second-harmonic generation measurements,

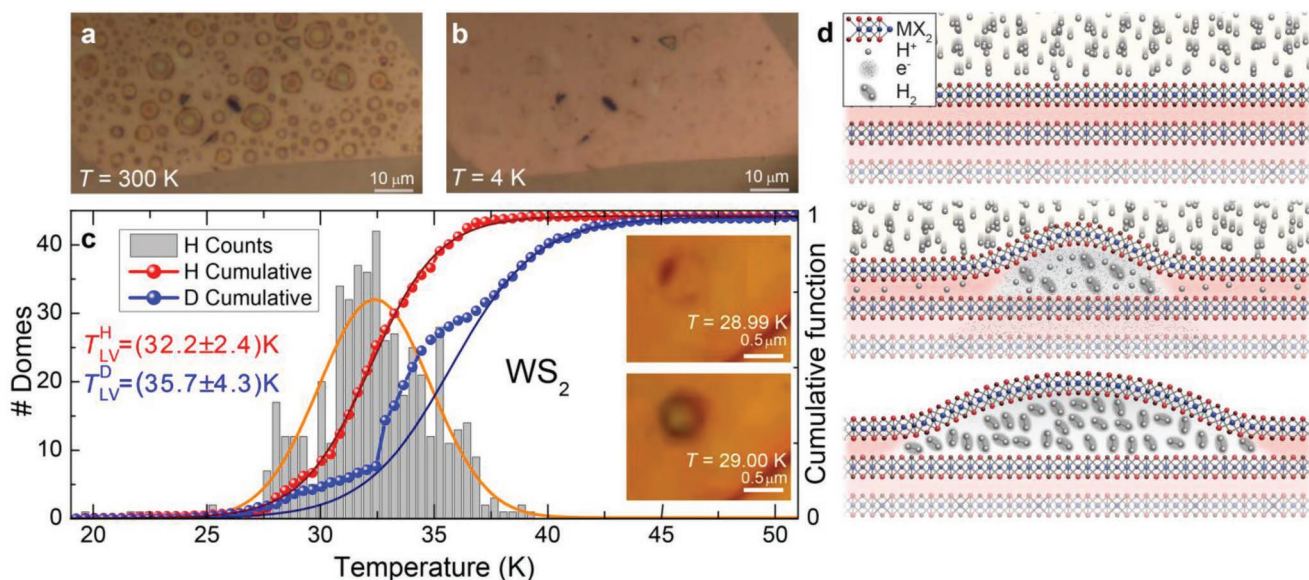


**Figure 2.** Dome inflating/deflating process. a) Optical microscopy image of an  $\text{H}^+$ -irradiated ( $d_{\text{H}} = 8 \times 10^{16}$  protons  $\text{cm}^{-2}$ )  $\text{WS}_2$  sample at  $T = 300$  K. b) Same as (a) at  $T = 4$  K. c) Histogram of the transition temperature at which domes appear (left axis). The orange line is a Gaussian fit to the data. The red point-line is the cumulative function of the histogram (right axis). The solid wine curve superimposed is a fit to the cumulative function providing the average transition temperature  $T^{\text{H}}_{\text{LV}}$  of proton-irradiated flakes. The blue point-line is the cumulative function of the histogram derived from deuteron-irradiated  $\text{WS}_2$  flakes and the corresponding navy fit providing  $T^{\text{D}}_{\text{LV}}$  is performed only on the part of the cumulative function in which H effects are negligible (see Note S1 in the Supporting Information). The insets are two optical microscopy pictures of the same dome, recorded immediately before (top) and after (bottom) the transition temperature. d) Sketch of the process leading to the formation of domes caused by the local blistering of atomically thin material membranes.

as discussed in the following. Albeit rare, the formation of two-layer thick domes and of Russian-doll-like structures can also be observed, as exemplified and discussed in Figure S5 in the Supporting Information.

Based on the percentage of visible domes that double as strong light emitters (see Figure S1 in the Supporting Information), at least 85%–90% of the domes can be estimated to be one-ML thick. The energy of the PL peak (corresponding to the free-exciton recombination involving electrons and holes at the  $K$  point of the first Brillouin zone, named as  $A$  exciton, as in TMD MLs<sup>[1,2]</sup>) of a typical (single-layer)  $\text{WS}_2$  dome is 200 meV lower than that of the ML (see Figure 1f), mainly because of the strain exerting on the dome's surface,<sup>[7,8]</sup> as we will discuss in more detail in the following. Notably, no significant linewidth broadening is observed when many such domes are measured together, as demonstrated by the PL spectrum of a dome ensemble, displayed in Figure 1f as a dashed line. The spectral homogeneity of the light emitted by the domes suggests that the same average strain is present in each dome, irrespective of the dome size. The evidence shown in Figure 1 demonstrates that indirect-gap bulk  $\text{WS}_2$  can be turned into an efficient light emitter with no size restrictions, like those typically affecting exfoliated flakes or samples grown by chemical vapor deposition. We point out that the reported phenomenon is substantially independent of the specific  $\text{MX}_2$  composition (see measurements on  $\text{H}^+$ -treated  $\text{MoSe}_2$ ,  $\text{MoS}_2$ ,  $\text{MoTe}_2$ ,  $\text{WSe}_2$ , and  $\text{WTe}_2$  in Figures S6 and S7 in the Supporting Information) and is exclusively induced by the interaction of the material with protons. No effect was found in samples exposed to molecular hydrogen or ionized helium atoms under the same temperature and gas flow conditions.

Clues on the internal make-up of the domes can be derived by following their low-temperature evolution. Figure 2a,b shows, respectively, the 300 and 4 K optical microscopy images of a bulk  $\text{WS}_2$  sample irradiated with  $d_{\text{H}} = 8 \times 10^{16}$  protons  $\text{cm}^{-2}$ . At 300 K, many domes—featuring iridescence, as accounted for below—are visible. For  $T \lesssim 30$  K the domes disappear, and the sample surface looks conspicuously flat. As  $T$  is increased, at  $\approx 30$  K, the domes bulge suddenly (within our system resolution equal to 10 mK, see insets of Figure 2c and Movie 1 (Supporting Information)). As illustrated in Figure 2c, the transition temperature distribution was sampled over more than 500 domes obtained on several proton-irradiated flakes deposited on different substrates (see the Experimental Section). The resulting average transition temperature is  $(32.2 \pm 2.4)$  K, a number close to the critical temperature of  $\text{H}_2$  (33.18 K) and thus compatible exclusively with the presence of molecular hydrogen inside the domes (see Note S1 in the Supporting Information): when  $T$  is sufficiently low/high,  $\text{H}_2$  liquefies/boils, and the domes deflate/inflate always in the same position.

The fluctuations in the liquid-vapor transition temperature ( $T^{\text{H}}_{\text{LV}}$ ) are chiefly due to the spread in the size (and hence in the internal pressure) of the domes. To reinforce our hypothesis, we considered the study of isotopic effects in our system and we repeated our analysis on 500 more  $\text{WS}_2$  domes, obtained by deuteron irradiation. The ( $p$ - $T$ ) phase diagrams of hydrogen and deuterium<sup>[20]</sup> show an isotopic shift in the temperature at which the liquid-vapor phase transition occurs of about 2.9 K (the exact value depending on the pressure of the gas). The details of our measurements are discussed in Note S1 in the Supporting Information. The cumulative function of

deuteron-irradiated samples is displayed in Figure 2c (see Figure SN1A for the histogram in the Supporting Information): differently from proton-irradiated samples, the behavior is in this case characterized by a composite shape, corresponding to the three different steps that are apparent in the cumulative function. We ascribe empirically these three steps to the presence of H<sub>2</sub>, HD, and D<sub>2</sub> molecules<sup>[21]</sup> within the domes. There are several possible explanations why H may be present also in deuterium-treated samples: (1) even the highest purity deuterium bottles contain a 0.25% of H<sub>2</sub> and HD molecules; (2) it has been reported that deuterons permeate through graphene and BN monolayers much slower than protons: At room temperature the areal conductivity of deuterons results to be 1/10 of that of protons.<sup>[22]</sup> This effect could be even much stronger in the case of TMDs, whose single layer is constituted by three atomic planes; (3) the hydrogen evolution reaction is expected to be remarkably faster with respect to the deuterium evolution reaction because of the high mass difference between the two isotopes.<sup>[23,24]</sup> For deuteron-irradiated samples, a sigmoidal fit was thus performed only to the high-temperature data of the cumulative function shown, where no effect from hydrogen is expected. The fit estimates a transition temperature of  $T_{LV}^D = (35.7 \pm 4.3)$  K, resulting in a difference between the centers of the distributions equal to  $(3.5 \pm 0.4)$  K, consistent with the (*p*-*T*) diagram of the two isotopes. Indeed, the measured transition temperatures are consistent only with the presence of H<sub>2</sub> (or its isotopes) within the domes (see Figure SN1B in the Supporting Information). We can therefore hypothesize that, during irradiation, accelerated protons penetrate through the top MX<sub>2</sub> basal plane (Figure 2d top), becoming confined in between two X-M-X layers. The penetration process is indeed ruled by the potential barrier met by protons at the interface with the bulk flake, which should be determined by both the binding energy profile of protons<sup>[25]</sup> and the electric fields/charges establishing at the sample surface.<sup>[26]</sup> Therein, likely triggered by the catalytic activity of TMDs, which might be similar to the electrocatalysis in aqueous solution,<sup>[14–16]</sup> the following reaction takes place



with electrons e<sup>-</sup> being supplied from the ground contact or possibly also from the bulk flakes themselves (Figure 2d middle). This hypothesis is supported by the fact that the formation of domes is strongly quenched in flakes deposited on an insulating substrate (Kapton tape). The subsequent build-up of H<sub>2</sub> molecules, stored just beneath the top surface, leads to the local blistering of one X-M-X plane, and eventually to the formation of the domes (Figure 2d bottom). The above scenario is supported by theoretical studies, which showed that thermal protons remain trapped in the metal plane of X-M-X layers and do not diffuse, thus favoring the accumulation of H<sub>2</sub> molecules in the interlayer regions.<sup>[25]</sup> An estimation of the number of molecules accumulated after irradiation (via AFM measurements and the mechanical model described in the following) indicates that <3% of the impinging protons penetrate and lead to the formation of molecular hydrogen, the remaining part likely being rejected by the potential barrier met at the sample surface, in agreement with previous studies concerning proton

irradiation of solid matrices.<sup>[27]</sup> The formation of localized nucleation sites (i.e., the domes), rather than the establishment of a uniform H<sub>2</sub> distribution underneath the top layer, is due to the van der Waals (vdW) forces existing between adjacent planes, which prevent H<sub>2</sub> molecules from moving freely. The shape of the domes itself—i.e., their height-to-radius ratio—results from the interplay between: (i) the vdW forces that tend to keep the TMD layers together, thus minimizing the dome radius; (ii) the stiffness of the top TMD layer, which limits the dome height; and (iii) the tendency to expand of the trapped gas, which results in the application of a constant pressure on the dome's walls.<sup>[6]</sup> We estimate such pressure to be about 10 atm for  $R \gtrsim 500$  nm, given the average  $T_{LV}^H = 32.2$  K and the H<sub>2</sub> phase diagram (see Note S1 and Ref. [20]). Therefore, the multicolored appearance of the large domes in Figure 2a can be ascribed to Newton's rings caused by the interference of the light reflected inside the H<sub>2</sub>-filled spherical volume.<sup>[28]</sup>

As noted earlier and shown in Figure 1f, the average PL peak energy of the domes is about 200 meV lower than that of the corresponding material in the ML form (see also Figure S7 in the Supporting Information). This is ascribable to the presence of tensile strain,  $\epsilon$ , which reaches its maximum  $\epsilon_m$  at the domes' summit. As predicted by Hencky's model<sup>[7,29,30]</sup>

$$\epsilon_m = f(\nu) \times (h_m/R)^2 \quad (2)$$

where *f* only depends on the material's Poisson ratio,  $\nu$ , while *R* and *h<sub>m</sub>* are the dome footprint radius and maximum height, respectively; see Note S2 in the Supporting Information. As reported in Ref. [6], the dome's height-to-radius ratio is largely independent of the dome's dimensions: *h<sub>m</sub>* scales linearly with *R*, and the value of  $\epsilon_m$  in a given material can be estimated by Equation (2). As shown in Figure 3a, wherein the experimental (i.e., obtained by AFM) values of *h<sub>m</sub>* are plotted as a function of *R* for six different chemical compositions, the expected linear dependence is verified over a wide span of dome sizes (*R* between 100 nm and  $\approx 3$   $\mu\text{m}$ ). The average values of *h<sub>m</sub>*/*R* estimated for each of the investigated materials are:  $0.16 \pm 0.02$  (MoS<sub>2</sub>),  $0.18 \pm 0.02$  (MoSe<sub>2</sub>),  $0.17 \pm 0.02$  (MoTe<sub>2</sub>),  $0.16 \pm 0.02$  (WS<sub>2</sub>),  $0.15 \pm 0.01$  (WSe<sub>2</sub>), and  $0.13 \pm 0.02$  (WTe<sub>2</sub>) yielding the values of  $\epsilon_m$  shown in Figure 3a and in Note S2 in the Supporting Information.

The height profile of the dome and the evolution of the strain tensor across the dome's surface can both be computed via finite-element method (FEM) calculations, performed within the framework of nonlinear membrane theory (see Note S3 in the Supporting Information).<sup>[29]</sup> As an illustrative case, Figure 3b (left) shows the comparison between these calculations and the AFM profile of a MoS<sub>2</sub> dome with  $R = (3.76 \pm 0.12)$   $\mu\text{m}$  and  $h_m = (618 \pm 15)$  nm, formed after irradiation of a flake with  $8 \times 10^{16}$  protons cm<sup>-2</sup>.

As summarized in Figure SN3A in the Supporting Information, FEM simulations correctly reproduce the experimental profile for all the investigated materials. The calculated spatial dependences ( $0 \leq r \leq R$ ) of the principal components of the strain tensor—namely, along the circumferential ( $\epsilon_r$ ) and radial ( $\epsilon_\theta$ ) in-plane directions<sup>[29]</sup> and along the perpendicular ( $\epsilon_z$ ) out-of-plane direction—are also displayed in Figure SN3A (right) (Supporting Information): interestingly, strain is isotropic

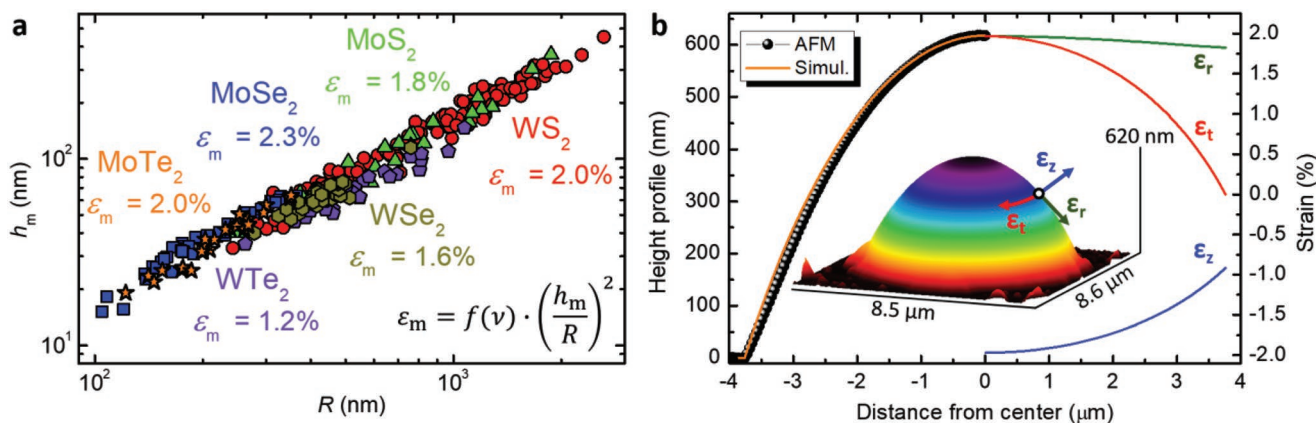


**Figure 3.** Dome's shape, strain, and size distribution. a) Maximum height  $h_m$  versus footprint radius  $R$  of  $\text{MX}_2$  domes. The average  $h_m/R$  provides the average dome biaxial tensile strain at the dome apex  $\varepsilon_m$ , according to the equation reported in the figure. b) Left axis: Comparison between the height profile of a  $\text{MoS}_2$  dome measured by AFM (black dots), and the profile obtained by finite elements calculations (solid orange line; see the Experimental Section). The dome footprint radius and height, as estimated by AFM measurements, are  $3.76 \mu\text{m}$  and  $618 \text{ nm}$ , respectively. Right axis: Components of the strain tensor along the three principal axes of the dome, i.e., in the radial ( $\varepsilon_r$ , solid olive line), circumferential ( $\varepsilon_t$ , solid red line), and perpendicular ( $\varepsilon_z$ , solid blue line) directions. These components are represented as color-coded arrows in the inset, showing a 3D AFM image of the dome.

biaxial ( $\varepsilon_t = \varepsilon_r = 1.97\%$  for the dome in Figure 3b) only at the very top of the dome, gradually becoming uniaxial as the circumferential component goes to zero near the dome's edge. In between these two limits, strain is anisotropic ( $\varepsilon_t \neq \varepsilon_r$ ), with a negative perpendicular component accounting for a compression in the out-of-plane direction (as detailed in Note S3 in the Supporting Information). The complex spatial dependence of the strain tensor across the domes is reflected by the spatial evolution of  $\mu$ -Raman measurements where, as a general feature, a progressive softening of the in-plane and out-of-plane vibrational modes is observed with increasing strain over the dome. Due to the diffraction-limited size of our laser spot (directly measured and modeled by a Gaussian with standard deviation  $\sigma = 0.23 \pm 0.01 \mu\text{m}$ , see the Experimental Section), the finer details of this evolution can only be appreciated on large ( $R > 2 \mu\text{m}$ ) domes:  $\mu$ -Raman measurements were therefore performed on  $\text{WS}_2$ ,  $\text{MoS}_2$ , and  $\text{WSe}_2$ , where large domes were fabricated, giving results in good agreement with the literature<sup>[7]</sup> discussed in Figures S8–S10 in the Supporting Information. Our results agree well also with Hencky's model,<sup>[7,29]</sup> yielding  $\varepsilon_m = \varepsilon_t = \varepsilon_r = 1.95\%$  for the  $\text{MoS}_2$  dome shown in Figure 3b (the same applies to the other  $\text{MX}_2$  compounds investigated; see Note S3 in the Supporting Information). Moreover, the pressure values used in the calculations match rather well, for  $\mu\text{m}$ -sized domes, with the  $\approx 10 \text{ atm}$  estimated from the average  $T^{\text{H}}_{\text{LV}}$  obtained in the previous section (see Figure 2c). For smaller ( $R \ll 1 \mu\text{m}$ ) domes, the model results in internal pressures in excess of  $100 \text{ atm}$ —as shown in Figure SN3B in the Supporting Information and reported in Ref. [6]—for which  $\text{H}_2$  should enter a supercritical fluid phase.<sup>[31]</sup>

The strain tensor evolution described by our model and confirmed by Raman measurements also allows the remarkable PL emission intensity characteristic of our domes as well as the PL energy position to be justified. The observed redshift is in fact quantitatively consistent with the estimated strain, as discussed for the  $\text{WS}_2$ ,  $\text{MoS}_2$ ,  $\text{WSe}_2$ , and  $\text{MoS}_2$  domes in Figure S7 in the Supporting Information. Due to the seamless reduction of the excitonic gap with increasing strain, on the other hand,

the formation of domes results in the creation of a deformation potential landscape for both electrons and holes, able to funnel the carriers towards the potential minima before recombining and thus giving rise to an enhanced PL emission. Such process, being at the origin of the bright luminescence observed in large electron–hole plasma droplets in locally strained germanium,<sup>[32]</sup> was also similarly observed in TMDs,<sup>[33,34]</sup> where excitons were demonstrated to drift for hundreds of nanometers before recombining.<sup>[34]</sup>

The detailed knowledge of the evolution of the strain tensor across the domes' surface is particularly relevant since strain is known to alter profoundly the electronic properties—and hence the optical and transport properties—of TMDs, which can lead to, e.g., the emergence of giant pseudo-magnetic fields and to the generation of persistent currents.<sup>[10–13]</sup> For this to happen, specific and stable configurations of the strain field need be achieved, and spatial control and durability are therefore necessary. In fact, other methods for the creation of strained TMD bubbles either allow size/position controllability but lack durability (as in Refs. [7,9]) or permit to create durable structures lacking any spatial ordering (as in Ref. [6]), in both cases considerably limiting their potentiality for applications.

As shown in Figure S11A in the Supporting Information, indeed, the domes created via proton-irradiation remain intact—and keep exhibiting strong light emission—for temperatures up to  $510 \text{ K}$ . In addition, the shape and size of these nano/microstructures remain unchanged with time—in the best cases over more than two years—as illustrated by Figure S11B–F in the Supporting Information. This confirms the notable absence of gas-permeable, nanometer-scale pores in TMD materials, as already reported in the literature;<sup>[7]</sup> moreover, the exceptional durability of our domes is likely also aided by the strong adhesion forces existing between the ML forming the dome and its parent substrate, as well as by the low permeability to  $\text{H}_2$  of the latter. In the bulging devices commonly employed to induce strain in TMD membranes<sup>[7–9]</sup> the ML is usually laying directly on a  $\text{SiO}_2$  substrate. As a result, the devices typically deflate within weeks, mostly due to leaks

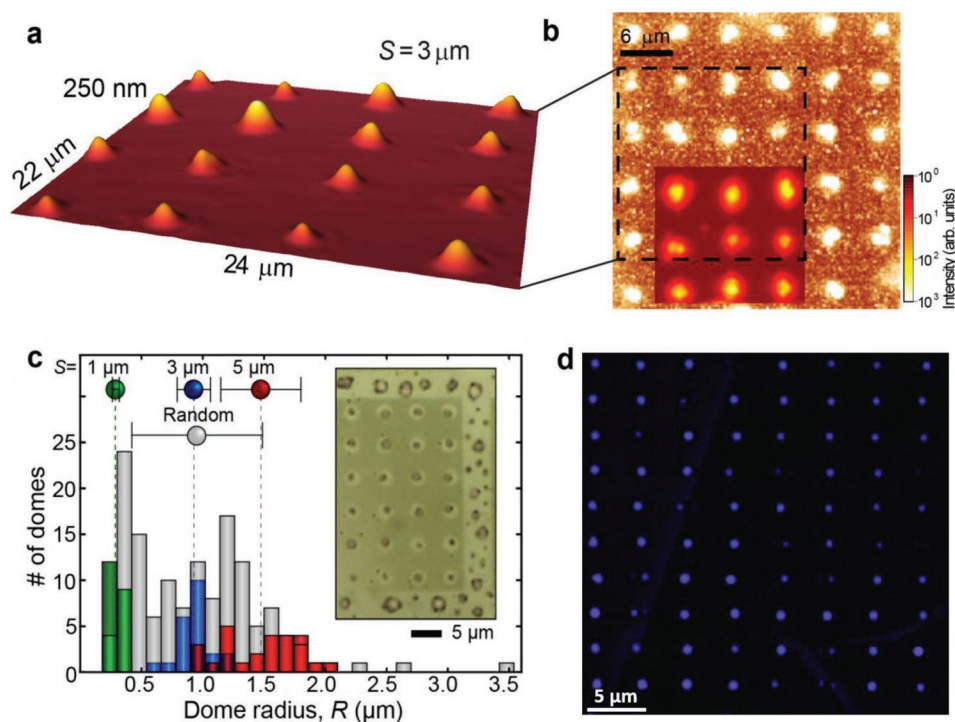


**Figure 4.** Controlling the dome size and position. a) AFM image of an array of WS<sub>2</sub> domes obtained after H<sup>+</sup> irradiation (dose  $d_H = 4 \times 10^{16}$  protons cm<sup>-2</sup>) of a flake patterned with an H-opaque mask. The mask had openings with diameter  $S = 3 \mu\text{m}$  and was removed before the AFM measure (see also Figure S13 in the Supporting Information). b) RT PL pan-chromatic imaging of the same array in (a) excited by a 532.2 nm laser. The bottom-left inset is a  $\mu$ -PL mapping (detection wavelength equal to 689 nm) of a portion of the same array. c) Distribution of the footprint radius of domes formed in opening arrays with diameter  $S = 1$  (green), 3 (blue), and 5 (red)  $\mu\text{m}$ . The distribution of randomly formed domes during the same process is given by gray bars. The distribution width is illustrated on top of the figure by horizontal bars. The inset is an optical microscopy image comparing random versus ordered ( $S = 3 \mu\text{m}$ ) domes. The much narrower distribution of the ordered domes with respect to the random ones can be appreciated. d) Second-harmonic (SHG) map collected on an array of ordered WS<sub>2</sub> domes obtained after proton irradiation (dose  $d_H = 1.5 \times 10^{17}$  protons cm<sup>-2</sup>) of a flake patterned with an H-opaque mask. The mask had elliptical openings with 2 and 1  $\mu\text{m}$  semiaxes and 4  $\mu\text{m}$  center-to-center distance.

through the substrate and the TMD/SiO<sub>2</sub> interface.<sup>[7]</sup> Besides durability, the applicative prospects of our MX<sub>2</sub> domes are greatly enhanced by the possibility to precisely control their size and position. The domes' formation process via low-energy proton-irradiation is indeed characterized by a high yield, the domes usually forming over the entire irradiated flakes, as shown in Figure S12 in the Supporting Information. This allows the dome formation process to be engineered, as illustrated in **Figure 4** that can be achieved by depositing an H-opaque masking layer prior to proton irradiation. The sample displayed in **Figure 4**, for example, was patterned by electron-beam lithography with arrays of circular openings with diameter  $S = 1, 3,$  and  $5 \mu\text{m}$  (see Figure S13 in the Supporting Information and Ref. [35]), followed by proton irradiation ( $d_H = 4 \times 10^{16}$  protons cm<sup>-2</sup>) and by the removal of the H-opaque mask (see the Experimental Section). **Figure 4a** displays the AFM image of a WS<sub>2</sub> array of neatly arranged single domes with average  $R = (0.93 \pm 0.07) \mu\text{m}$  and  $h_m = (0.13 \pm 0.02) \mu\text{m}$ , obtained for  $S = 3 \mu\text{m}$ . The  $\mu$ -PL signal emitted by the same array is imaged in **Figure 4b** (see also the  $\mu$ -PL map in the inset). The ability to fabricate ordered arrays of light-emitting domes is an inherent advantage of our system with respect to, e.g., the bubbles forming because of the accidental incorporation of contaminant gases between monolayers and their supporting substrates,<sup>[6,36]</sup> which have been shown to be durable<sup>[37]</sup> but lack any spatial

ordering. The dome dimensions can also be engineered by varying the size of the openings in the H-opaque mask. In fact, **Figure 4c** shows the distributions of the dome footprint radii grouped into randomly formed and ordered dome subsets obtained during the same proton-irradiation process. It is worth noting that the domes formed using the lithographic approach are characterized by a remarkably narrower size distribution, where the size is clearly determined by the diameter of the aperture. Such distribution gets even narrower with decreasing the dome size. Finally, in the ordered arrays, the average dome volume scales with the surface area ( $0.25\pi S^2$ ) available to the reaction (1) (see Figure S14 in the Supporting Information), thus supporting the hypothesis of the dome formation as a catalysis-driven process. We point out that controlling the dome position and size over large areas is valuable for the creation of efficient site-controlled photon emitters, as well as in many other situations. For example, TMD MLs have been shown to give rise to efficient second-harmonic generation (SHG), due to their broken inversion symmetry.<sup>[38,39]</sup> This property is retained by our domes—as demonstrated in **Figure 4d** for an ordered array of WS<sub>2</sub> domes excited at 900 nm, which could thus conceivably act as site-controlled SHG “hot spots,” ideal for the integration with specifically designed photonic crystal cavities.<sup>[40,41]</sup> One should also notice that the intense second-harmonic signal featured

by the domes in Figure 4d indicates a >96% formation yield of one-ML-thick domes.

ML TMDs have been demonstrated to possess intriguing optoelectronic and mechanical properties, which render them suitable for flexible and innovative optoelectronic devices. Furthermore, they have emerged as a fascinating class of materials for catalysis.<sup>[15]</sup> While irradiation of these materials with energetic (MeV) beams has been shown to modify their properties due to the creation of defects,<sup>[18]</sup> here we demonstrated that irradiating bulk TMD flakes with a low energy proton flux leads to the formation and accumulation of hydrogen and enables the control of the electronic properties of ML TMDs at the nano- and micro scale through the creation of light-emitting, highly strained domes. The irradiation process proposed here therefore allows the morphological and optical properties of the flakes to be altered without the creation of defects (as demonstrated by the stability of the domes, see Figure S11 in the Supporting Information, and by optical measurements, see Figure S15 in the Supporting Information), resulting into relatively large areas characterized by efficient light emission, due to the creation of the domes. These structures can be formed at the desired location and with controllable size on six different compounds. Since we can precisely control the amount of H<sub>2</sub> in single domes, they can act as microscopic calibration gauges for H<sub>2</sub> sensors or for controlled delivery of reactive gas (see Figure S16 in the Supporting Information) in nanoreactors<sup>[42]</sup> with unprecedented accuracies. The engineered formation of domes also allows the creation of arrays of linear and nonlinear light emitters and of periodic strain fields, as here demonstrated. Finally, it should be noted that several other 2D crystals—such as graphene, h-BN, and phosphorene—have been found to be virtually transparent to protons, according to both experiments<sup>[43]</sup> and theoretical calculations.<sup>[25]</sup> Therefore, their deposition on top of bulk TMD samples before proton irradiation should not hinder the dome formation process, and the controlled formation of (ordered) TMD domes could thus be exploited to define a template for modulating strain in a much wider range of 2D materials, leading, e.g., to the emergence of giant pseudo-magnetic fields in graphene. Thanks to the spatial control enabled by our method, these latter could be created in the desired periodic configurations, which have been predicted to result in the generation of dissipation-less electrical currents.<sup>[10–13]</sup>

## Experimental Section

An extensive description of sample preparation and proton irradiation procedure, of phase transition, optical, and structural measurements, and of sample patterning can be found in the Supporting Information.

## Supporting Information

Supporting Information is available from the Wiley Online Library or from the author.

## Acknowledgements

D.T. and E.B. contributed equally to this work. The authors gratefully acknowledge A. Miriametro for valuable technical support. The authors

are grateful to P. Postorino, E. Lavrov, and J. Weber for discussions about molecular hydrogen detectability by Raman spectroscopy. The authors thank: E. Cappelluti for useful discussion about the electronic properties of TMDs; R. Canteri, D. Giubertoni, and G. Pepponi for secondary ion mass spectrometry measurements; S. Albano for preliminary sample preparation; and A. Notargiacomo for support during AFM measurements. The authors thank J. Avila, G. Avvisati, and M. G. Betti for X-ray photoelectron spectroscopy measurements. The authors thank M. Capizzi, G. Ciasca, C. Jagadish, F. Martelli, and A. Surrente for discussions. The authors acknowledge Centro di ricerca per le nanotecnologie applicate all'ingegneria - CNIS. The authors acknowledge support by Sapienza Università di Roma under the "Avvio alla Ricerca 2016" (D. T.) and "Ricerche Ateneo" (A.P. and M.F.) grants. M.F. and G.P. acknowledge support and funding from the Italian Ministry for Education, University and Research within the Futuro in Ricerca (FIRB) program (project DeLIGHTeD, Prot. RBF12RS1W). This project has also received funding from the European Union's Horizon 2020 research and innovation program No. 641899. The authors acknowledge funding support from Australian Research Council (ARC) (numbers DE140100805 and DP180103238), and ARC Centre of Excellence in Future Low-Energy Electronics Technologies (project number CE170100039). A.P. and M.F. acknowledge funding from the Regione Lazio programme "Progetti di Gruppi di ricerca" legge Regionale n. 13/2008 (SINFONIA project, prot. n. 85-2017-15200) via LazioInnova spa. D.T., E.B., M.F., and A.P. fabricated the domes, performed and designed the optical experiments, and conducted the analysis regarding the optical and microscopy data. E.B. performed and analyzed the isotopic shift measurements. G.P. designed and performed the sample lithographic processing and the microscopy measurements. T.Y. and Y.L. made the mechanical modeling calculations. E.P. and S.S. contributed at the initial stages of this work. B.L., C.Z., Y.Z. prepared the samples and performed part of the optical experiments. Y.L. coordinated the work at the Australian National University. A.P. and M.F. wrote the manuscript. A.P. conceived the research and coordinated the work at Sapienza Università di Roma. All authors discussed the results and commented on the manuscript.

## Conflict of Interest

The authors declare no conflict of interest.

## Keywords

hydrogen evolution reaction, photoluminescence, Raman, strain, transition-metal dichalcogenides, 2D materials

Received: June 14, 2019

Revised: August 24, 2019

Published online: September 23, 2019

- [1] L. Zhang, A. Zunger, *Nano Lett.* **2015**, *15*, 949.
- [2] S. Z. Butler, S. M. Hollen, L. Cao, Y. Cui, J. A. Gupta, H. R. Gutierrez, T. F. Heinz, S. S. Hong, J. Huang, A. F. Ismach, E. Johnston-Halperin, M. Kuno, V. V. Plashnitsa, R. D. Robinson, R. S. Ruo, S. Salahuddin, J. Shan, L. Shi, M. G. Spencer, M. Terrones, W. Windl, J. E. Goldberger, *ACS Nano* **2013**, *7*, 2898.
- [3] X. Li, L. Tao, Z. Chen, H. Fang, X. Li, X. Wang, J.-B. Xu, H. Zhu, *Appl. Phys. Rev.* **2017**, *4*, 021306.
- [4] A. Pospischil, T. Mueller, *Appl. Sci.* **2013**, *6*, 78.
- [5] F. Schwierz, J. Pezoldt, R. Granzner, *Nanoscale* **2015**, *7*, 8261.
- [6] E. Khestanova, F. Guinea, L. Fumagalli, A. Geim, I. Grigorieva, *Nat. Commun.* **2016**, *7*, 12587.
- [7] D. Lloyd, X. Liu, J. W. Christopher, L. Cantley, A. Wadehra, B. L. Kim, B. B. Goldberg, A. K. Swan, J. S. Bunch, *Nano Lett.* **2016**, *16*, 5836.

- [8] R. Yang, J. Lee, S. Ghosh, H. Tang, R. M. Sankaran, C. A. Zorman, P. X.-L. Feng, *Nano Lett.* **2017**, *17*, 4568.
- [9] D. Lloyd, X. Liu, N. Boddeti, L. Cantley, R. Long, M. L. Dunn, J. S. Bunch, *Nano Lett.* **2017**, *17*, 5329.
- [10] F. Guinea, M. I. Katsnelson, A. K. Geim, *Nat. Phys.* **2010**, *6*, 30.
- [11] M. Casalilla, H. Ochoa, F. Guinea, *Phys. Rev. Lett.* **2014**, *113*, 077201.
- [12] H. Ochoa, R. Zarzuela, Y. Tserkovnyak, *Phys. Rev. Lett.* **2017**, *118*, 026801.
- [13] M. Taillefumier, V. K. Dugaev, B. Canals, C. Lacroix, P. Bruno, *Phys. Rev. B* **2008**, *78*, 155330.
- [14] T. F. Jaramillo, K. P. Jørgensen, J. Bonde, J. H. Nielsen, S. Horch, I. Chorkendorff, *Science* **2007**, *317*, 100.
- [15] D. Voiry, J. Yang, M. Chhowalla, *Adv. Mater.* **2016**, *28*, 6197.
- [16] D. Kiriya, P. Lobaccaro, H. Y. Y. Nyein, P. Taheri, M. Hettick, H. Shiraki, C. M. Sutter-Fella, P. Zhao, W. Gao, R. Maboudian, J. W. Ager, A. Javey, *Nano Lett.* **2016**, *16*, 4047.
- [17] R. Trotta, A. Polimeni, F. Martelli, G. Pettinari, M. Capizzi, L. Felisari, S. Rubini, M. Francardi, A. Gerardino, P. C. M. Christianen, J. C. Maan, *Adv. Mater.* **2011**, *23*, 2706.
- [18] G.-Y. Zhao, H. Deng, N. Tyree, M. Guy, A. Lisfi, Q. Peng, J.-A. Yan, C. Wang, Y. Lan, *Appl. Sci.* **2019**, *9*, 678.
- [19] G. Sallen, L. Bouet, X. Marie, G. Wang, C. R. Zhu, W. P. Han, Y. Lu, P. H. Tan, T. Amand, B. L. Liu, B. Urbaszek, *Phys. Rev. B* **2012**, *86*, 081301.
- [20] A. S. Friedman, D. White, H. L. Johnston, *J. Am. Chem. Soc.* **1951**, *73*, 1310.
- [21] H. J. Hoge, R. D. Arnold, *J. Res. Natl. Bur. Stand.* **1951**, *47*, 75.
- [22] M. Lozada-Hidalgo, S. Hu, O. Marshall, A. Mishchenko, A. N. Grigorenko, R. A. W. Dryfe, B. Radha, I. V. Grigorieva, A. K. Geim, *Science* **2016**, *351*, 68.
- [23] T. Green, D. Britz, *J. Electroanal. Chem.* **1996**, *412*, 59.
- [24] C. Korte, T. Mandt, T. Bergholz, in *Physics of Hydrogen*, Vol. 2, (Eds: D. Stolten, B. Emonts), Wiley-VCH, Weinheim, Germany **2016**, p. 566, Ch. 24.
- [25] M. Seel, R. Pandey, *2D Mater.* **2016**, *3*, 025004.
- [26] a) C. H. Seager, in *Hydrogen in Semiconductors*, Vol. 34 (Eds: J. I. Pankove, N. M. Johnson), Academic Press Limited, London, UK **1991**, pp. 17–33, Ch. 2; b) A. D. Marwick, in *Hydrogen in Semiconductors*, Vol. 34 (Eds: J. I. Pankove, N. M. Johnson), Academic Press Limited, London, UK **1991**, p. 220, Ch. 9.
- [27] R. Trotta, D. Giubertoni, A. Polimeni, M. Bersani, M. Capizzi, F. Martelli, S. Rubini, G. Bisognin, M. Berti, *Phys. Rev. B* **2009**, *80*, 195206.
- [28] S. J. Cartamil-Bueno, P. G. Steeneken, A. Centeno, A. Zurutuza, H. S. J. van der Zant, S. Houry, *Nano Lett.* **2016**, *16*, 6792.
- [29] P. Wang, W. Gao, Z. Cao, K. M. Liechti, R. Huang, *J. Appl. Mech.* **2013**, *80*, 040906.
- [30] W. B. Fichter, *NASA Tech. Pap.* **1997**, 3658, 1.
- [31] C. Korte, T. Mandt, T. Bergholz, in *Physics of Hydrogen*, Vol. 2, (Eds: D. Stolten, B. Emonts), Wiley-VCH, Weinheim, Germany **2016**, p. 570, Ch. 24.
- [32] C. D. Jeffries, *Science* **1975**, *189*, 955.
- [33] J. Feng, X. Qian, C.-W. Huang, J. Li, *Nat. Photonics* **2012**, *6*, 866.
- [34] A. Castellanos-Gomez, R. Roldan, E. Cappelluti, M. Buscema, F. Guinea, H. S. J. van der Zant, G. A. Steele, *Nano Lett.* **2013**, *13*, 5361.
- [35] S. Birindelli, M. Felici, J. S. Wildmann, A. Polimeni, M. Capizzi, A. Gerardino, S. Rubini, F. Martelli, A. Rastelli, R. Trotta, *Nano Lett.* **2014**, *14*, 1275.
- [36] D. A. Sanchez, Z. Dai, P. Wang, A. Cantu-Chavez, C. J. Brennan, R. Huang, N. Lu, *Proc. Natl. Acad. Sci. USA* **2018**, *115*, 7884.
- [37] A. V. Tyurnina, D. A. Bandurin, E. Khestanova, V. G. Kravets, M. Koperski, F. Guinea, A. N. Grigorenko, A. K. Geim, I. V. Grigorieva, *ACS Photonics* **2019**, *6*, 516.
- [38] N. Kumar, S. Najmaei, Q. Cui, F. Ceballos, P. M. Ajayan, J. Lou, H. Zhao, *Phys. Rev. B* **2013**, *87*, 161403.
- [39] C. Janisch, Y. Wang, D. Ma, N. Mehta, A. L. Elías, N. Perea-López, M. Terrones, V. Crespi, Z. Liu, *Sci. Rep.* **2015**, *4*, 5530.
- [40] M. S. Mohamed, A. Simbula, J.-F. Carlin, M. Minkov, D. Gerace, V. Savona, N. Grandjean, M. Galli, R. Houdré, *APL Photonics* **2017**, *2*, 031301.
- [41] M. Minkov, V. Savona, D. Gerace, *Appl. Phys. Lett.* **2017**, *111*, 131104.
- [42] S. H. Petrosko, R. Johnson, H. White, C. A. Mirkin, *J. Am. Chem. Soc.* **2016**, *138*, 7443.
- [43] S. Hu, M. Lozada-Hidalgo, F. C. Wang, A. Mishchenko, F. Schedin, R. R. Nair, E. W. Hill, D. W. Boukhvalov, M. I. Katsnelson, R. A. W. Dryfe, I. V. Grigorieva, H. A. Wu, A. K. Geim, *Nature* **2014**, *516*, 227.